Laboratory experiments on the effects of corrosion inhibitor on the mechanical properties of reservoir rock

Kortram, Jon Danilo; Barnhoorn, Auke; Pluymakers, Anne

DOI
10.1186/s40517-023-00257-3

Publication date
2023

Document Version
Final published version

Published in
Geothermal Energy

Citation (APA)
Kortram, J. D., Barnhoorn, A., & Pluymakers, A. (2023). Laboratory experiments on the effects of corrosion inhibitor on the mechanical properties of reservoir rock. *Geothermal Energy*, *11*(1), Article 17. https://doi.org/10.1186/s40517-023-00257-3

Geothermal Energy

RESEARCH Open Access

Laboratory experiments on the effects of corrosion inhibitor on the mechanical properties of reservoir rock

Jon-Danilo Kortram[1*], Auke Barnhoorn[1] and Anne Pluymakers[1]

*Correspondence:
jondanilokortram@gmail.com

[1] Department of Geoscience and Engineering, Delft University of Technology, PO-box 5048, 2600 GA Delft, the Netherlands

Abstract

Geothermal energy production often involves use of corrosion inhibitors. We performed rock mechanical experiments (room temperature; confining pressure of 10/20/30 MPa) on typical reservoir rocks (Bentheim sandstone and Treuchtlinger limestone) in contact with two different inhibitor solutions or with demineralized water. The sandstone experiments show no discernible difference in rock strength between inhibitors or water, attributed to low quartz reactivity. The limestone experiments show a significant difference in rock strength (and Mohr–Coulomb envelope), dependent on inhibitor type, attributed to high carbonate reactivity. This implies that, depending on the reactivity of the rocks and local stress conditions, inhibitor leakage may lead to unpredicted reservoir failure.

Highlights

- Triaxial tests of Bentheim sandstone and Treuchtlinger limestone are done at ~20°C.
- Mohr-Coulomb envelope for sandstone not affected by inhibitors (3000 ppm).
- Limestone strength oppositely affected by 2 inhibitors compared to water.
- Sandstone reservoirs no change in risk of failure due to inhibitor leakage.
- Limestone reservoir show an increased risk of failure due to inhibitor leakage.

Keywords: Corrosion inhibitor, Physical rock properties, Rock–fluid interaction, Experimental rock mechanics

Introduction

Many low to moderate temperature geothermal systems in sedimentary aquifers comprise either sandstone or limestone reservoir rocks (Buijze et al. 2019). For example, in North-West Europe, geothermal systems in limestone reservoirs are common in the Molasse basin (Moeck et al. 2020) and the Paris basin (Regnet et al. 2015). Currently, the majority of Dutch geothermal systems are in sandstone reservoirs, and limestone

formations are promising targets for future systems (Boxem et al. 2015; Dutch Association of Geothermal Operators (DAGO) 2018). In geothermal operations, hydrothermal fluid is extracted from the subsurface. This produced fluid can contain corrosive species (Nogara and Zarrouk 2018). When the steel well casing, or other parts of the geothermal plant come into contact with this fluid, they can deteriorate due to corrosion (e.g., Mundhenk et al. 2013). This can lead to production problems and may require costly workovers. To prevent such problems, geothermal operators typically apply corrosion inhibitors. These inhibitors are designed to retard or prevent the chemical interactions leading to corrosion (Kelland 2014). A type of corrosion inhibitor that is often applied in geothermal operations is the film-forming corrosion inhibitor (e.g., Ghaziof et al. 2018; Huttenloch et al. 2021; Watering and Veld 2019). This type of inhibitor adsorbs to the metal surface and forms a protective barrier that physically prevents corrosive chemicals from contact and interaction with the metal surface (McMahon 1991). Many film-forming corrosion inhibitors are organic amphiphiles (surfactants) with a nitrogen-based polar headgroup and an apolar carbon-based hydrophobic tail (Watering and Veld 2019). The polar head interacts with the iron atoms on the surface. The tails will interact with components in the fluid, and form a film to create a barrier to the corrosive elements (Kelland 2014). When used in a production scenario, corrosion inhibitors are continuously injected in the production well (Watering and Veld 2019). This way the protective inhibitor film can form along the fluid path. When corrosion inhibitor is applied in geothermal operations, the injected concentration is usually up to 15 parts per million (ppm), and there is a small risk of inhibitor solution leaking into the geothermal reservoir (Watering and Veld 2019). It would be beneficial to know if there is an additional mechanical danger involved with corrosion inhibitors seeping into the reservoir given how frequently they are used. If a chemical agent would alter the absolute strength of the reservoir rock, unexpected fracturing could occur. This in turn has the potential to increase permeability, and thereby uncertainty with respect to doublet lifetime. Moreover, the fracturing of rock may lead to induced seismicity which has been a reason to discontinue production in numerous locations (Buijze et al. 2019).

Fracturing of rock is governed by stress-induced growth of micro-cracks and flaws, as described by Griffith's theory of fracture (Jaeger et al. 2007). As these flaws grow, they link together with other flaws to form macroscopic fractures, which is supported by both microstructural analysis of rock samples in different failure stages (e.g., Barnhoorn et al. 2010; Bruno and Nelson 1991; Hallbauer et al. 1973) and the high amount of microfractures observed near macroscopic fractures (Fossen 2010). The strength of a rock is thereby controlled by the initial presence of flaws and nucleation points of cracks, and how easily these flaws grow into a macroscopic fracture. Rock strength is usually affected by the presence of water. Generally speaking, limestone rocks (i.e., calcite based) are more reactive and soluble (Sjöberg and Rickard 1984) than sandstone rocks (i.e., quartz based) (Rimstidt and Barnes 1980). Despite this general inertness of quartz, sandstone rock strength is usually (but not always) reduced when the rock is in contact with water (up to 39%, see Baud et al. 2000; Hadizadeh and Law 1991; Heap et al. 2018). For sandstones, the strength reduction is commonly attributed to the reduction in specific surface-free energy, especially in clay-rich sandstones (Heap et al. 2018). Sandstones are mostly negatively charged at the surface (Hilner et al. 2015; Shehata et al. 2015).

Mechanical testing of sandstone at room temperature using brines representative for geothermal sandstone reservoirs showed no additional effects of brine composition (relative to the water-wet strength) (Heap et al. 2018). Limestone often shows water-weakening (up to 30%, see amonst others, Castagna et al. 2018; Lisabeth and Zhu 2015; Rutter 1972a), and brines are shown to have an additional mechanochemical effect (Heggheim et al. 2005; Madland et al. 2011; Megawati et al. 2013; Pluymakers et al. 2021). The presence or absence of a mechanochemical effect is generally attributed to the reactivity of the constituents and their chemical reactivity (e.g., solubility) in the presence of water. For instance, water-weakening by dissolution and precipitation can strongly affect the mechanical rock strength. This process is controlled by the presence of common ions in the brine solution (Heggheim et al. 2005). However, not all changes in mechanical limestone rock behaviour can be attributed to dissolution or mineral reactions even though the exact nature of the involved mechanisms are not yet fully understood (Pluymakers et al. 2021). A limestone surface is usually slightly positively charged (Bassioni and Taha Taqvi 2015), and experiments on chalk in combination with brines suggest that ion adsorption to the mineral surface alters the surface charge which impacts the mechanical behaviour (Megawati et al. 2013).

Given the importance of limestone and sandstone reservoirs for the geothermal industry, the frequent use of inhibitors and the different potential for mechanochemical effects of these common reservoir rocks, we set out to experimentally investigate how exposure to two commonly used corrosion inhibitors affects the mechanical properties of sandstone and limestone rocks. The tested specimens are analogues to geothermal reservoir rocks. Since these inhibitors are specifically aimed at adsorption and the formation of fluid films on material surfaces, we hypothesize they could be capable of influencing the mechanical behaviour of rocks as well, which in the end is governed by interactions between mineral surfaces. To our knowledge, there is no literature regarding any interaction between rocks and inhibitor fluids, even though the consequences are potentially significant. Therefore, we have performed standard triaxial compressive tests on representative sandstone and limestone rocks in combination with demineralized water or inhibitor solutions. Comparable triaxial tests have been performed on reservoir rock analogues (e.g., Egert et al. 2018; Rudnicki 2004; Rutter and Glover 2012; Zhu et al. 1997). In this work, we use an exaggerated inhibitor concentration of 3000 ppm and two different commercially available corrosion inhibitors.

Methodology

We performed standard compressive triaxial tests on Treuchtlinger Marmor (limestone) and Bentheim sandstone samples. All experiments are listed in Table 2. For each rock type, we performed three test series using different fluid solutions for each series: DI water, commercial inhibitor type 1 and type 2 (see Table 3 for the compositions of inhibitor type 1 and 2). In each series experiments were performed at a confining pressure of 10, 20 or 30 MPa and room temperature (approximately 20 °C).

In our experiment, the inhibitor concentration is high compared to the injection rate used by field operators in geothermal operations. These high concentrations could occur if the inhibitor agent accumulates in the reservoir, as mentioned by Zotzmann et al. (2018). In this section, we propose a back-of-the-envelope calculation (Eq. 1) to

demonstrate how long it would take for the inhibitor to accumulate to a concentration equal to our test concentration of 3000 ppm. In this scenario, we assume that all the corrosion inhibitor that is injected at the production well will eventually reach the reservoir at the same concentration of 15 ppm, i.e., a worst-case scenario where no inhibitor reacts inside the wellbore. As a consequence, the injected fluid will spread out radially from the wellbore in the reservoir. Since corrosion inhibitor is specifically designed to adsorb to solid surfaces, we assume that it adsorbs and accumulates near the wellbore, both vertically and laterally. We assume it spreads vertically in a layer with a thickness of 10 m, and that it will adsorb laterally to the reservoir rock within a 50 m radius of the injection well. We furthermore assume that the reservoir is homogenous and that all pores are connected. These assumptions then leads to the following simple equation describing the time (T) it takes for the inhibitor accumulation to reach our test concentration.

$$T = \frac{\left(\pi \times r^2 \times h \times \varphi\right)}{\left(q_i \times c_i\right)} \times c_d (365 \times 24)^{-1} \tag{1}$$

where r is the deposition radius of the inhibitor, h is the reservoir height, ϕ is the reservoir porosity, q_i is the production and injection rate, c_i is the concentration of the injected corrosion inhibitor, and c_d is the corrosion inhibitor concentration in the subsurface. Values for all these variables in Eq. 1 are listed in Table 1. The reservoir and operation parameters in our calculation are of a similar order of magnitude to the models described by e.g., Daniilidis et al. (2021). The corrosion inhibitor dose is obtained from Watering and Veld (2019). Using these numbers provides an estimate that it could take approximately 2.7 years for the inhibitor to accumulate to the downhole concentration used in our experiment.

The Bentheim Sandstone is used as an example reservoir analogue for potential sandstone geothermal reservoirs, and the Treuchtlinger Marmor as an example reservoir analogue for potential carbonate geothermal reservoirs (Dinantian). Note that the Dinantian carbonates are geothermal targets in the Netherlands (Boxem et al. 2015), and Upper Jurassic carbonate rock is a geothermal target in the southwest Bavarian Molasse Basin in Germany (Mijnlieff 2020). All samples had a diameter of 29.6 mm, and a length of ~ 60 mm, i.e., a length to diameter ratio of 2:1. Samples ends were polished to be plane-parallel within 100 µm. Increased porosity exerts a large weakening influence on rock strength (Baud et al. 2014; Carbillet et al. 2021; Zhang et al. 1990). Before testing, the porosity of each individual sample was measured with a He-pycnometer after 24 h + of drying in a 60 °C oven.

Table 1 list of variables used in the calculation of the corrosion inhibitor accumulation

Variable	*Symbol*	Value
Production and injection rate	q_i	100 m^3/hr
Reservoir thickness	h	10 m
Reservoir porosity	φ	15%
Corrosion inhibitor deposition radius	r	50 m
Corrosion inhibitor dose	c_i	15 ppm
Final downhole inhibitor concentration	c_d	3000 ppm

The Bentheim Sandstone is a member of the Vlieland Sandstone formation (Early Cretaceous) (Dubelaar and Nijland 2015). This formation is of Valanginian age. It is a quartz-rich (> 90%) sandstone with minor amounts of feldspar and clay, and trace amounts of pyrite and other iron minerals (Klein et al. 2001; Peksa et al. 2015). Grain size has been reported to be homogenously distributed, with a median grain size 200–330 μm (Peksa et al. 2015). It is considered a homogeneous sandstone. Our samples exhibited a narrow range of porosity of 26–27.3%. Bentheim sandstone is a well-characterized sandstone, which has been frequently used in rock mechanics experiments (e.g., Bakker and Barnhoorn 2019; Blöcher et al. 2014; Klein et al. 2001; Klein and Reuschle 2003; Peksa et al. 2015). After performing the deformation experiment a selection of samples were made into thin sections. These sections were analyzed using transmitted light microscopy. A part of the sample far away from the main damage zone is used as an indication of the microstructure of the starting material (Fig. 1a). Based on the thin sections, the samples consist mainly of monocrystalline quartz with trace amounts of opaque minerals, likely hematite or goethite (< 1%). It is a moderately sorted sandstone, with most grains ranging from 0.1 mm to 0.5 mm. The grains have a subangular to subrounded shape, with occasional traces of fluid inclusions and/or microcracks. These observations are in line with the description given in Peksa et al. (2015). Repeatability experiments show a maximum strength variation of only 4.2 MPa, which is less than < 4% of sample strength.

The Treuchtlinger Marmor is also known as Jura-Marmor, Jura-Kalkstein and Treuchtling Marble. Despite the name "Treuchtlinger Marmor", this rock is actually of sedimentary origin (Niebuhr and Pürner 2014). The Treuchtlingen Formation belongs to the Late Jurrasic (Middle Kimmeridgian, also known as the White Jura) (Mönnig 2006). In outcrop, it is light-yellow to blue-grey, fossil-rich and fine-grained. It is characterized by thick and well-bedded silicate-sponge biostromes with abundant Tubiphytes (Koch and Weiss 2005). An example of the initial microstructure is shown in Fig. 1b. The Treuchtlinger Marmor samples used in this experiment were collected from an abandoned quarry near Ingolstadt, Germany. Carbonates are often highly heterogeneous, and to ensure sample-to-sample-comparability, all samples are hand-picked from adjacent blocks to be similar in looks, porosity and density. Initial porosity was between 7.7 and 10.3%. Repeatability experiments show a strength variation of only 2–5 MPa, which is less than < 3.5% of sample strength.

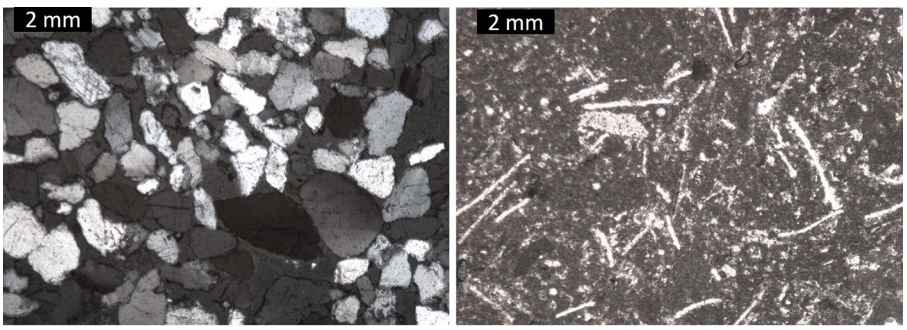

Fig. 1 Overview thin section starting material, obtained from thin sections of damaged samples but taken far away from the damage zone, for **a** Bentheim sandstone (BS-09) and **b** Treuchtlinger Marmor (TM2-3)

The fluids used were either demineralised water, or solutions made with one of the two inhibitor solutions at 3000 ppm. This concentration was accomplished in two steps of weight-based dilution of the pure inhibitor with demineralised water. First, 10 g (g) inhibitor was mixed with 90 g demineralised water, and 30 g from the resulting mixture was mixed with 970 g of demineralised water.

One day prior to testing, four oven-dry samples were immersed in a beaker filled with 500 millilitre (ml) of the targeted fluid (i.e., demineralised water, inhibitor 1 or inhibitor 2). The beaker filled with the submerged samples was then placed in a vacuum desiccator and left under vacuum for approximately 30 min, until no more bubbles appeared, taken as the sign of saturation. The bath was covered with several layers of cling film, ensuring no evaporation could take place, and the samples were left at room conditions for 16 to 24 h. Note that during this time minor calcium carbonate ($CaCO_3$) dissolution can take place, which could potentially slightly weaken the samples (Lisabeth and Zhu 2015). To check if a chemical reaction occurred (dissolution or precipitation), the pH value of the solutions was measured before and after the overnight saturation period, using measurement strips with a resolution of ± 0.5. Post-bathing, pre-experimental sample weighing indicated that the porosity reached 75–100% saturation. Prior to testing the inhibitor 1 solution had a pH of 6.5 and the solution of inhibitor 2 had an initial pH of 5.5. For the sandstone no change in pH was measured, indicating that no dissolution took place. For the limestone samples, a change in pH was measured after the overnight saturation period. The pH of both solutions increased to 7.0.

To perform the triaxial tests, we used a commercially available Hoek cell (Hoek and Franklin 1968), loaded into a loading frame equipped with an internal load cell with a range of 500 kN. An external direct displacement syringe pump (ISCO 65D) controls the confining pressure inside the Hoek cell with 0.5% accuracy. Piston displacement was measured using two high-precision linear variable differential transformers with a 2 mm range (LVDT). After the saturation period, the sample was placed inside the Hoek cell and the loading frame. Once the Hoek cell was in place, LVDT's were placed and the confining pressure and axial load were increased in an alternating fashion. The axial load was kept between 1.4 and 4.2 MPa above the confining pressure (i.e., within the elastic regime of both sample types). Once the targeted confining pressure was reached, the sample was left to settle for ~ 15 min. The experiment began by loading the sample at a constant displacement rate, which coincided with an axial strain rate of 10^{-5} s^{-1}. During the experiment the relative piston displacement, the axial force, the confining pressure and the fluid flow-rate from the ISCO pump were logged at 1 s intervals. All experiments were performed under drained conditions without additional pore fluid pressure. As a result the compressive action did not affect pore pressure, and the resulting stress equals the effective stress. Loading continued until the measured axial load dropped abruptly, indicating that macroscopic sample failure occurred. As soon as the samples failed, the unloading process was initiated, which followed a procedure opposite to the loading process. This method is, therefore, not suitable to study the effect of fluid on post-peak residual strength of these samples. During unloading, axial load was kept approximately 7.1 MPa above the confining pressure. Once a confining pressure of 0.3 MPa was reached, the sample was unloaded and demounted. The samples were removed as carefully as possible. After every test run, any part that had been in contact with pore-fluid

was thoroughly cleaned with demineralized water and ethanol, and afterwards dried, to ensure no cross-contamination of pore fluids.

Note that, though the Hoek cell has advantages in terms of quick sample placement and operability, slight modifications in microstructure due to removal of the sample from the sleeve cannot be excluded, as the samples may be further damaged as they are removed from the sleeve. Our microstructural efforts pertained mainly to the limestone samples due to the significant mechanochemical effect of fluids. Selected samples are scanned post-experimentally with a NanoTom microtomography-scanner (commonly referred to as a CT-scanner). In a CT-scanner, x-rays are used to obtain a non-invasive internal image of the scanned objects. We used an operating voltage of 180 kV and a current of 0.5 mA. The images have a voxel size of $(28\ \mu m)^3$ or $(56\ \mu m)^3$. The following samples were scanned: BS-17 (voxelsize 28 µm), TM2-4 (voxelsize 56 µm), TM2-5 (voxelsize 56 µm) TM2-8 (voxelsize 28 µm), TM3-6 (voxelsize 28 µm) and TM3-1 (voxelsize 56 µm). Sample BS-09 (P_c 20 MPa, tested with water), TM4-2 (P_c 20 MPa, tested with water), TM2-2 (P_c 20 MPa, tested with inhibitor 1) and TM2-3 (P_c 20 MPa, tested with inhibitor 2) are impregnated with blue epoxy resin, and imaged using optical light microscopy.

Compressive stress and compressive axial strain are defined as positive. The principal normal stresses are denoted as σ_i with $\sigma_1 > \sigma_2 = \sigma_3 = P_c$ where σ_1 is the axial stress and P_c is the confining pressure. The differential stress is denoted as $\sigma_{\text{diff}} = \sigma_1 - \sigma_3$. The rock strength is defined as the peak differential stress $(\sigma_{\text{diff}})_{\text{max}}$. The axial strain is the ratio of the change in sample length over the original sample length. The axial strain is denoted as $\epsilon_1 = dL/L_0$. The slope of the linear part of the stress—strain curve is used to determine the Young's Modulus (denoted as E). We have used the Mohr–Coulomb failure criterion to characterize the experimental results, defined by $|\tau| = S_0 + \mu\sigma_n$, where τ is the shear stress, S_0 stands for the cohesion, and μ is the coefficient of friction and σ_n is the normal stress (Jaeger et al. 2007).

Results

Sandstone

The stress–strain curves are shown in Fig. 2. At all confining pressures, failure occurred brittle, marked by an abrupt drop in the axial load. Values for strength and Young's Modulus are given in Table 2. The values for the sandstone Young's modulus range from 21.6 to 25.1 GPa, without any dependence on fluid type and a slight positive trend with increasing confining pressure. Repeat experiments were performed at 10 MPa for inhibitor 1 and 2, and the range in sandstone rock strength at this confining pressure is 4 MPa, less than 3.5% of peak strength. At all confining pressures, the variation of rock strength between the different fluids is within this range, independent of fluid type.

The Mohr–Coulomb failure criteria for all three fluid types are constructed with the peak stresses (Fig. 3). The corresponding values for S_0 are 20 ± 3; 18 ± 3 and 19 ± 3 MPa, respectively, for demineralised water, inhibitor 1 and inhibitor 2. The friction coefficient μ is 0.80 ± 0.07; 0.80 ± 0.07 and 0.81 ± 0.06, respectively. From these results, it is clear that the exposure to inhibitor 1 or inhibitor 2 compared to exposure to demineralised water had no discernible effect on any of the mechanical rock parameters, which is in line with the lack of change to the pH during the overnight bath.

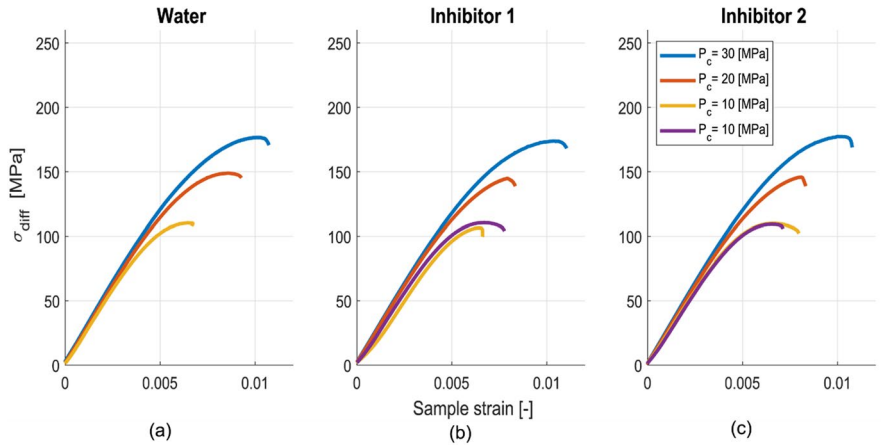

Fig. 2 Sample strain (axial) versus differential stress (σ_{diff}) curves for Bentheim sandstone samples, obtained at different confining pressures (P_c). Legend is the same for all three panels and shown in panel **c**. To improve readability, the repeat experiments (performed at 10 MPa) are assigned a purple colour instead of yellow. Stress–strain curves are not influenced by fluid type. **a** sandstone with water; **b** sandstone with inhibitor 1 (3000 ppm); **c** sandstone with inhibitor 2 (3000 ppm)

Table 2 Experimental conditions and main characteristics of all experiments

Sample number	Fluid	P_c [MPa]	Porosity [%]	Density (kg/m^3)	$(\sigma_{diff})_{max}$ [MPa]	E [GPa]	S_0 [MPa]	μ [−]	CT/TS
Bentheim sandstone									
BS-05	DI	30	26.5	2.03	176.7	24.5	20 ± 3	0.80 ± 0.07	
BS-09	DI	20	26.9	2.03	148.9	24.1			TS
BS-07	DI	10	26.7	2.03	110.3	23.5			
BS-04	1	30	26.0	2.06	173.8	24.6	18 ± 3	0.80 ± 0.07	
BS-01	1	20	26.8	2.02	144.8	24.4			TS
BS-10	1	10	27.3	2.01	106.5	21.6			
BS-11	1	10	26.7	2.01	110.7	23.1			
BS-17	2	30	27.1	2.02	177.3	25.1	19 ± 3	0.81 ± 0.06	
BS-16	2	20	26.6	2.01	145.9	24.5			
BS-15	2	10	27.2	2.01	110.1	23.2			
BS-14	2	10	26.6	2.05	109.4	23.4			
Treuchtlinger marmor									
TM3-6	DI	30	8.8	2.52	205.6	49.7	33 ± 5	0.67 ± 0.07	CT
TM4-2	DI	20	10.3	2.53	180.2	42.5			TS
TM4-1	DI	10	10.2	2.55	152.9	43.9			CT
TM2-4	DI	10	8.3	2.53	157.2	50.1			CT
TM2-8	1	30	8.3	2.56	217.4	46.6	59 ± 10	0.43 ± 0.11	CT
TM2-2	1	20	7.8	2.53	201.9	39.1			TS
TM2-5	1	10	8.8	2.56	191.4	46.6			CT
TM2-6	2	30	7.7	2.51	241.8	52.7	23 ± 3	1.01 ± 0.05	
TM2-3	2	20	8.5	2.52	205.9	45.3			TS
TM3-1	2	10	8.3	2.48	146.9	39.1			
TM2-7	2	10	8.7	2.49	148.2	45			

E is the Youngs Modulus, S_0 the cohesion and μ the friction coefficient obtained from the Mohr–Coulomb failure criterion. TS and CT indicate whether 'thin sections' or 'computerized tomographic scans' were made, respectively

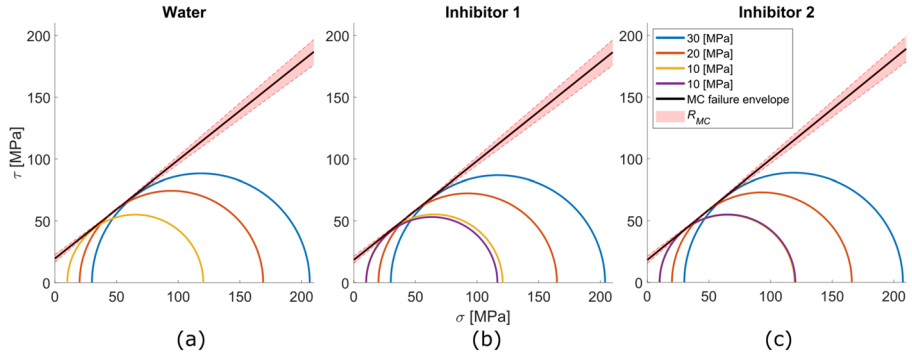

Fig. 3 Mohr–coulomb failure envelopes on shear stress (τ) versus normal stress (σ) plots for Bentheim sandstone. Legend is the same for all three panels. The pink area labelled R_{MC} indicates the uncertainty which was estimated based on the repeat experiments. Slope (friction coefficient μ ~ 0.8, see Table 2) and intercept (cohesion S_0 ~ 19 MPa, see Table 2) are unaffected by fluid type. **a** sandstone with water; **b** sandstone with inhibitor 1 (3000 ppm); **c** sandstone with inhibitor 2 (3000 ppm)

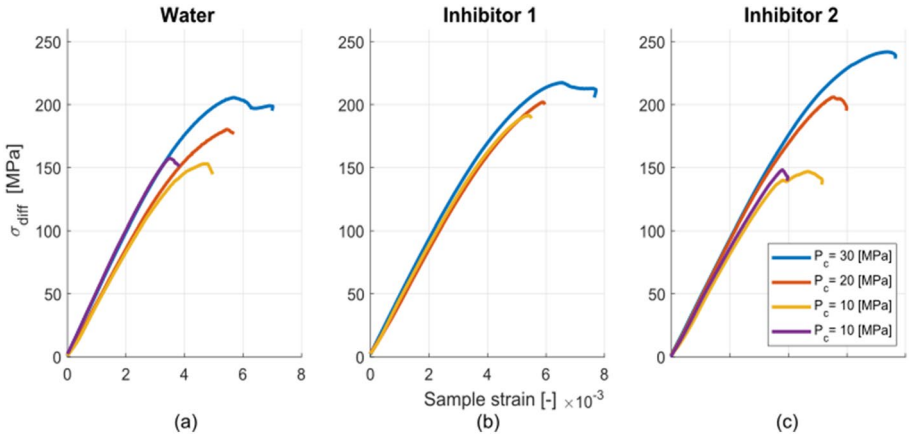

Fig. 4 Sample strain (axial) versus differential stress (σ_{diff}) curves for the Treuchtlinger Marmor limestone samples, obtained at different confining pressures (P_c). Legend is the same for all three panels and shown in panel c. To improve readability, the repeat experiments (performed at 10 MPa) are assigned a purple colour instead of yellow. Stress–strain curves are significantly influenced by fluid type, with different effects depending on the confining pressure. **a** Limestone with water; **b** Limestone with inhibitor 1 (3000 ppm); **c** Limestone with inhibitor 2 (3000 ppm)

Limestone

The stress–strain curves are shown in Fig. 4. Sample failure occurred brittle at all confining pressures, marked by an abrupt drop in the axial load. Values for strength and Young's Modulus are given in Table 2. The Young's Modulus varies between 39 and 53 GPa, without a clear dependence on fluid type or confining pressure. The repeatability was tested at 10 MPa on samples saturated with water and with inhibitor 2, and was within 4 MPa (less than 3% of the sample strength at this confining pressure). Sample strength depends systematically on confining pressure and fluid type (see Fig. 4), where at 10 MPa samples saturated with inhibitor 2 are weaker, followed by water, followed by inhibitor 1. At 20 MPa, water-saturated samples are weakest, followed by inhibitor 1 and 2, which exhibit almost equal strength. At 30 MPa, water-saturated samples remain weakest, followed by inhibitor 1, and samples saturated with inhibitor

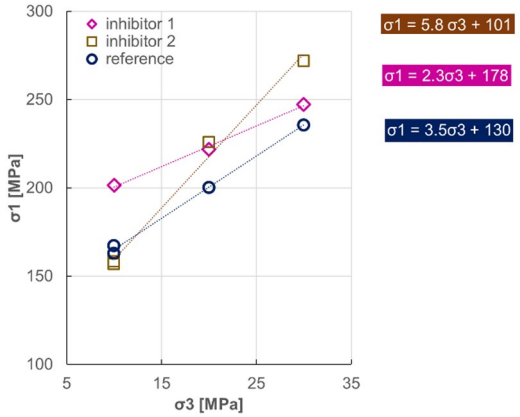

Fig. 5 σ_1-σ_3 plot for the limestone samples, showing different trends for the relationship between σ1 and σ2 depending on the pore fluid

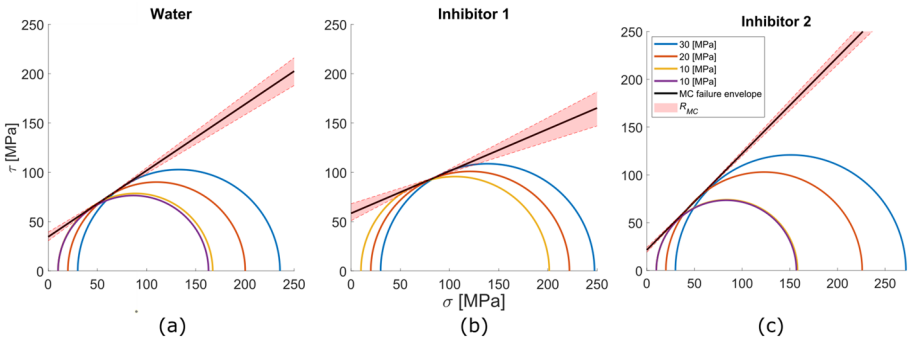

Fig. 6 Mohr–coulomb failure envelopes on shear stress (τ) versus normal stress (σ) plots for Treuchtlinger Marmor limestone. Legend is the same for all three panels. The pink area labelled R_{MC} indicates the uncertainty which was estimated based on the repeat experiments. **a** limestone with water, with a cohesion of 33 ± 5 MPa and a friction coefficient of 0.67 ± 0.07; **b** limestone with inhibitor 1 (3000 ppm), with a cohesion of 59 ± 10 MPa and a friction coefficient of 0.43 ± 0.11; **c** limestone with inhibitor 2 (3000 ppm), with a cohesion of 23 ± 3 and a friction coefficient of 1.01 ± 0.05

2 or the strongest in the dataset. For all three fluid types the peak stress depends linearly on the confining pressure (Fig. 5).

The Mohr–Coulomb failure criteria (Fig. 6) for limestone in contact with the three fluid types are constructed with the peak stresses from the stress–strain curves. The corresponding values for S_0 are 33 ± 5; 59 ± 10 and 23 ± 3 MPa, respectively, for water, inhibitor 1 and inhibitor 2. The friction coefficient μ is 0.67 ± 0.07; 0.43 ± 0.11 and 1.01 ± 0.05, respectively. Exposure to inhibitor 1 or inhibitor 2 compared to water each had a significant and opposite effect on the Mohr–Coulomb parameters. Compared to water, the exposure to inhibitor 1 increased the cohesion and decreased the friction coefficient, whereas inhibitor 2 decreased the cohesion and increased the friction coefficient. Prior to testing, the inhibitor 1 solution had a pH of 6.5 and the solution of inhibitor 2 had an initial pH of 5.5. After the overnight saturation period the pH value of both solutions increased to 7.0, indicating that minor dissolution has taken place in both samples, and the samples exposed to inhibitor 2 experienced more dissolution than those exposed to inhibitor 1.

Optical microscopy

Sandstone tested with water

Since there is no effect of fluid on failure mode or mechanical strength, only one sandstone sample has been extensively analysed. Sample BS-09 has been chosen as the representative sample for the mechanical behaviour of the Bentheim samples. The fracture consists of a central damage zone, surrounded by a symmetric zone up to 2 mm wide of increased density of intragranular micro-cracks, see Fig. 7a. The central damage zone is up to 500 µm wide and consists of a gouge with micrometre-sized grains, i.e., a strong grain size reduction compared to the starting material, and intensely fractured. The grains in the damage zone contain more micro-cracks than

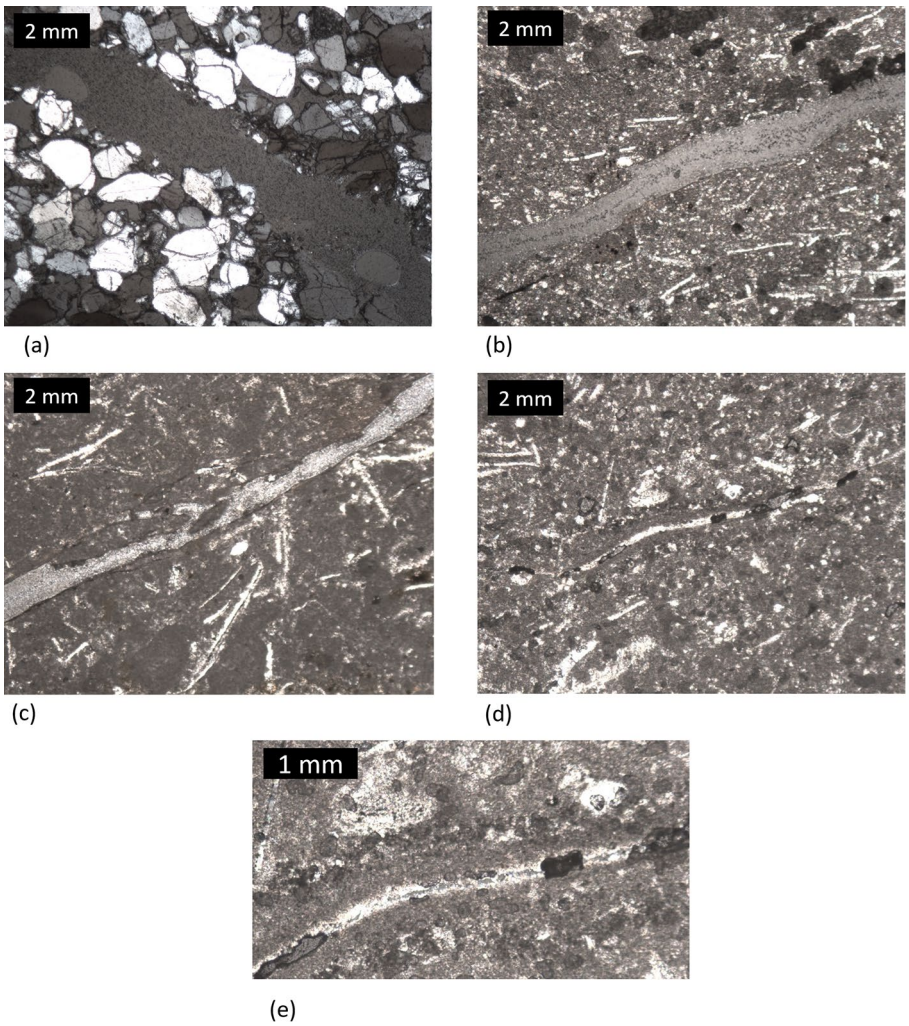

Fig. 7 Microstructures of samples deformed at 20 MPa confining pressure, all obtained with under cross-polarized light. **a** BS-09, Bentheim sandstone deformed with water. **b** TM4-2, Treuchtlinger Marmor limestone deformed in the presence of water. Gouge-filled localized shear-zone with boundary shear zones, about 100 µm wide. **c** TM2-2, Treuchtlinger Marmor limestone deformed in the presence of inhibitor 1 (3000 ppm). Incohesive sample, visible, intact, islands in main shear zones, seperated by highly localized fractures, and minimal gouge development. **d** TM2-3, Treuchtlinger Marmor limestone deformed in the presence of inhibitor 2 (3000 ppm). **e** TM2-3 shown at a greater magnification to show the fracture and damage zone

the starting material, most of which originate and terminate on the grain contacts. This type of cracks are a typical result of grain-on-grain contact and are classified as Hertzian fractures (Fischer-cripps 2000).

Limestone tested with water

Sample TM4-2, tested at 20 MPa, is taken as the representative sample for the Treuchtlinger Marmor tested with DI water, i.e., the reference sample. The fracture is a localized zone of fault gouge of approximately 100 µm width, where in one ~ 600 µm stretch (Fig. 7b) the entire zone has been preserved. This shows that inside this damage zone there are boundary shear zones, as well as occasional localized zones with a 20° angle to the shear zone boundaries, resembling the orientation in Riedel shear zones. There are no clear displacement indicators along the shear zone. The fracture aperture varies but appears to be no greater than 0.3 mm, where the residual gouge is present irregularly and with variable thickness.

Limestone tested with inhibitor 1

Sample TM2-2, tested at 20 MPa, is taken as the representative sample for Treuchtlinger Marmor tested in the presence of inhibitor 1 (3000 ppm). At this confining pressure, this sample exhibits a higher peak stress than the reference sample tested with water. There is no visible damage zone near the main fracture, and the sample has completely split, i.e., there is epoxy separating the two sides of the fracture. The edges of the fracture appear dark, taken as an indication of grain size reduction and strain localization. Even when residual parts of the damage zones remain as islands separated by anastomosing fracture branches, no gouge formation is visible, instead there are pieces of fractured wall-rock without visible grainsize reduction in an epoxy matrix (Fig. 7c).

Limestone tested with inhibitor 2

Sample TM2-3, tested at 20 MPa, is taken as the representative sample for Treuchtlinger Marmor tested in the presence of inhibitor 2 (3000 ppm). At this confining pressure, this sample is similar in strength as TM2-2. The fracture is a narrow highly localized zone, partly infiltrated and separated with epoxy, with grains and air bubbles at irregular intervals. Zooming in on the intact parts of the damage zone, it is a highly localized zone up to 20 µm in width, with dark edges assumed to be boundary shear zones. There is minimal gouge development, and larger calcite grains can contain abundant microcracks of variable orientation (Fig. 7d).

To sum up, both inhibitors exhibited a difference in both cohesion and friction coefficient in the Mohr–Coulomb criterion compared to DI water, where inhibitor 1 increased the cohesion and decreased the friction coefficient, and inhibitor 2 did the inverse. Even though on the scale of microtomography (Fig. 9 in Appendix I) there are no obvious differences in microstructure, the greater detail provided by the optical microscope shows a correlation between microstructure and fluid type. Going from

water to inhibitor 1 to inhibitor 2, gives a decreasing amount of grain size reduction and an increase in localization.

Discussion

The abrupt failure, combined with the microstructural evidence, indicates that all samples (sandstone and limestone) failed in a brittle manner. Moreover, all experiments show that an increased confining pressure results in increased rock strength, which is expected within the brittle field for both sandstone (Heap et al. 2009; Yang et al. 2012) and limestone (e.g., Rutter 1972a, b; You 2010). Note that, in experimental rock mechanics, when testing under confining pressure, the use of three experiments per condition is frequently done (Baud et al 2000; Castagna et al 2018; Lisabeth and Zhu 2015), especially when samples are from a narrow porosity range (e.g., Descamps et al. 2012). There is no discernible difference in the mechanical rock properties for the Bentheim sandstone when comparing the samples that were saturated with water to the samples that were saturated with one of the inhibitors. However, there was a significant difference for the Treuchtlinger Marmor samples. In the following, we will first discuss potential reasons for the lack of response in Bentheim sandstone, followed by potential reasons for the significant effects observed in Treuchtlinger Marmor. This will be followed by a discussion on the implications of the results for geothermal reservoirs.

Sandstone

In most environments at or near the Earth's surface, especially at temperatures up to 100 °C or so (i.e., medium temperature geothermal heat), quartz is considered to be chemically inert (Mackenzie and Gees 1971; Rimstidt and Barnes 1980). Therefore, the lack of change in mechanochemical properties of sandstone upon exposure to high inhibitor concentrations of 3000 ppm can be attributed to the chemical inertness of the prevalent quartz minerals in the Bentheim sandstone. Our results imply that even if inhibitor leaks into a sandstone reservoir at low temperatures (i.e., with low chemical reactivity) no mechanochemical consequences are expected.

However, the adsorption kinetics of organic matter to quartz depend on factors such as the ionic strength, the nature of divalent cation, the pH, the adsorbent content and the temperature (Jada et al. 2006), where a change from 20 to 40 or 60° increases the sorption of organic matter significantly. When sorption of natural organic matter occurs, it can lead to a modification of the surface charge (Jada et al. 2006). The change in sandstone strength in the presence of water is usually considered to be the result of a change in surface interactions (Atkinson and Meredith 1981; Heap et al. 2018). Therefore, we postulate that the sorption of inhibitors may lead to changes in sandstone strength under those conditions where the quartz surface would be reactive. This indicates that the inhibitor-sandstone interactions in high enthalpy reservoirs or reservoirs with initially complex pore fluids (in terms of salinity or pH) would require additional research.

Limestone

The different inhibitors have different chemical compositions (Table 3), and could therefore exhibit different inhibitor-limestone reactions. Given that only the limestone samples were affected by inhibitors, potential factors that may alter rock strength are likely related to the chemical reactivity of carbonate, the main component of limestone. In the following, we will discuss first why sample heterogeneity and uniform dissolution cannot explain these results, followed by a discussion on the potential effects of local dissolution, grain contact lubrication and zeta potential.

Limestone is often highly heterogeneous. However, there are three reasons why we consider the change in strength to be a true effect and not a consequence of heterogeneous samples. First, a careful sample selection, using samples within 2% porosity (Helium-pycnometry as well as density-based calculations) combined with a visual inspection, created a homogenous sample batch. This is confirmed by the lack of correlation between sample strength and measured porosity and/or density. Second, repeat experiments were performed at 10 MPa for samples saturated with water, and for samples saturated with inhibitor 2, and strength fell within 4 MPa, whereas the differences between the fluid types were 10–50 MPa, i.e., 5–25%, which is significant and comparable to the magnitudes previously reported for water-weakening in sandstones and limestones. For comparison, water-weakening in sandstones is reported by Baud et al (2000) to be 5–17%, for low strain rates and 200 MPa confining pressure up to 15%, and Heap et al (2018) showed that sandstones in a geothermal reservoir exhibited 24–39% water-weakening. For limestone, Castagna et al. reported 10–30% weakening on Comiso limestone and Rutter (1972a, b) showed up to 30% weakening on Solnhofen limestone. Changes in strength due to the presence of different chemistry were shown to be up to ~ 25% due to the presence of carbonate ions (Lisabeth and Zhu 2015), 50% due to the presence of $MgSO_4$ (Pluymakers et al. 2021). Third, there is a strong positive correlation between σ_1 and σ_3 (Fig. 5), which shows a systematic change in mechanical strength that also correlates with observable differences in post-failure microstructures.

Table 3 Composition of the inhibitors, labelled here inhibitor 1 and inhibitor 2

Product/ingredient name	Weight %
Inhibitor 1	
Ethoxylated amine salt	$10 \leq \ldots \leq 25$
1,2-ethaandiol	≤ 10
2-(2-butoxyethoxy)ethanol	≤ 10
Quaternairy ammoniumcompounds, benzyl-alkyldimethyl-, chlorides	≤ 5
Inhibitor 2	
Pyridinium, 1-(fenylmethyl)-,ethylmethylderivates, chlorides	$10 \leq \ldots \leq 25$
Thio-ureum	≤ 5
Alcohols, C8-10, ethoxylated	≤ 3
Propaan-2-ol	≤ 3
Alkyl dimethylbenzyl ammonium chloride ADBAC/BKC (C12-16)	≤ 1

The ethoxylated amine salt is a nitrogen-based compound, as is the thio-ureum. Pyridinium is the conjugate acid of pyridine, which is often used as an organic base in chemical reactions. The general structure of the inhibitors is a polar head with a long non-polar tail

The experiments were performed with pre-saturated samples without any additional fluid pressure. Therefore, any reaction that occurs would probably take place before the experiment starts. Since both inhibitor-enriched fluids are slightly acidic. An obvious candidate to change the sample microstructure and thereby strength would be uniform dissolution during the saturation time. During the saturation process for both inhibitors, the pH value increased slightly, indicating some carbonate is dissolved. Prior to testing, the inhibitor 1 solution had a pH of 6.5 and the solution of inhibitor 2 had an initial pH of 5.5. After the overnight saturation period, the pH value of both solutions increased to 7.0. The sample dimensions and weight (roughly 100 g) and the quantity of fluid used (around 500 ml for four samples) were similar for both datasets. The dissolution of carbonate occurs according the following set of reactions:

$$CaCO_3\,(s) + H_2CO_3\,(aq) \leftrightarrow Ca^{2+}\,(aq) + 2HCO3^{-}\,(aq) \tag{2}$$

$$HCO3^{-}\,(aq) \leftrightarrow CO3^{2-}\,(aq) + H^{+}\,(aq) \tag{3}$$

Combining these two equations shows that each mole of solid carbonate that dissolves leads to 2 mol of H^+ in solution. Using the pH changes that were measured, with a 0.5 pH of measurement error, means that for inhibitor 1 the pH changes (from 6–6.5 to 7) can be explained if in each sample 1.3 to 5.6 µgr of carbonate dissolves. For inhibitor 2 (pH changes from 5–6 to 7) per sample 5.6–61.9 µgr needs to dissolve. With an initial weight of ~ 100 g this means < 0.1% overall porosity change per sample. Dissolution means the porosity increases. Multiple authors note an inverse relationship between rock strength and porosity, which makes intuitive sense: a higher porosity would mean there is less rock material to support applied load, effectively increasing the force on the individual rock particles (Hoshino 1974; Kelsall et al. 1986; Pvrikryl 2001). A change in porosity has been cited before as the cause for sample weakening (Arson and Vanorio 2015; Clark and Vanorio 2016; Lisabeth and Zhu 2015; Vialle and Vanorio 2011). If samples would simply have been uniformly weakened due to uniform dissolution by contact with either inhibitor solution, one would expect uniform weakening at all confining pressures, and/or potentially a decrease in cohesion for the different inhibitors compared to water. Even though the pH change indicates that for both inhibitor solutions very minor dissolution occurred, inhibitor 1 samples actually exhibit an increase in cohesion. Combining this with the minor amount of sample material that dissolved makes uniform dissolution highly unlikely as a potential explanation for the observations.

Local dissolution can lead to crack tip blunting. Rostom et al. (2013) performed in low-velocity crack propagation experiments in single calcite crystals. They suggested that calcite dissolution may cause crack tip blunting, which explains the slowdown of crack growth and which could potentially strengthen samples. If this occurred in our Treuchtlinger Marmor samples during the saturation process before the experiment, the existing microcracks in the limestone could become blunter, and it would become less easy for cracks to start to grow. During brittle failure the microstructure normally evolves in three stages (Hoek and Martin 2014), where (i) at 40–60% of peak stress new

cracks initiate; (ii) at 60–70% stable crack growth occurs; and (iii) at 70–90% unstable crack growth commences, leading to failure. The mechanism of crack tip blunting does not affect the number of crack nucleation points, it only impedes crack propagation. As such this mechanism has the potential to affect peak stress differently at each confining pressure. It also implies a negligible effect on elasticity, since only the shape of the nucleation points of cracks is changed. It could also explain why the final microstructures show different amounts of fault gouge. This could potentially explain our observations.

The corrosion inhibitors used in our experiments are designed to form a fluid film on solid surfaces. These inhibitors have a different composition, and thereby the fluid film (if it indeed forms in limestone) would potentially have different characteristics. In these rock mechanics experiments, the different inhibitors affect not only cohesion but also the slope of the Mohr–Coulomb envelope. This slope gives the friction coefficient as well as the angle of internal friction, which suggests that the inhibitors have the potential to change intergranular lubrication, perhaps via a change of local viscosity due to the water being confined in the pores (Bowen and Yousef 2003). This could potentially alter the friction coefficient between granular contacts. A similar effect is observed in wet chalks and shales. Water is drawn and held in pore spaces by strong capillary forces created by surface bonding energies and water surface tension. Thin water films separate the grains, and the motion in mobile fluid layers promotes grain movement (Dobereiner and De Freitas 1986; Morgenstern et al. 1974). On the basis of these experiments, there are no grounds to fully reject this hypothesis. It should be noted here that before the experiment, the porosity in these rocks is 75–100% filled with fluid, and there is no fluid reservoir connected to the samples. This means that as soon as cracks grow or new cracks open, there is very little driving mechanism towards wetting the newly created surfaces, apart from surface interactions. Newly formed cracks are, therefore, potentially not fully wet. This would explain why there is no effect of the inhibitor on the failure dynamics itself in this study (i.e., no change in failure class type I or II, such as reported by Pluymakers et al. 2021).

Another potential difference between the inhibitors and demineralized water could be the zeta potential at the rock–liquid interface. A film-forming corrosion inhibitor, which potentially adsorbs to the solid surface, could also affect the electric double layer in the first nanometres of fluid at the rock–fluid interface. This may also change the forces between the limestone rock particles, and a similar mechanism was postulated before for limestone-brine interactions (Megawati et al. 2013; Pluymakers et al. 2021) However, to reject or accept this hypothesis direct zeta potential measurements should be made, which is outside the scope of this manuscript.

Implications for limestone reservoirs

Production fluid temperatures are 60–100 °C in the Netherlands (Watering and Veld 2019), and temperature is a controlling factor on zeta potential, rock deformation behaviour and the rates of most chemical reactions [usually according to the Arrhenius law (e.g., Connors 1990)]. However, for limestone in particular, carbonate solubility (and therefore reactivity) decreases with an increase in temperature (Plummer and Busenberg 1982). This means that performing experiments at room temperature provides, reactivity-wise, a worst-case scenario.

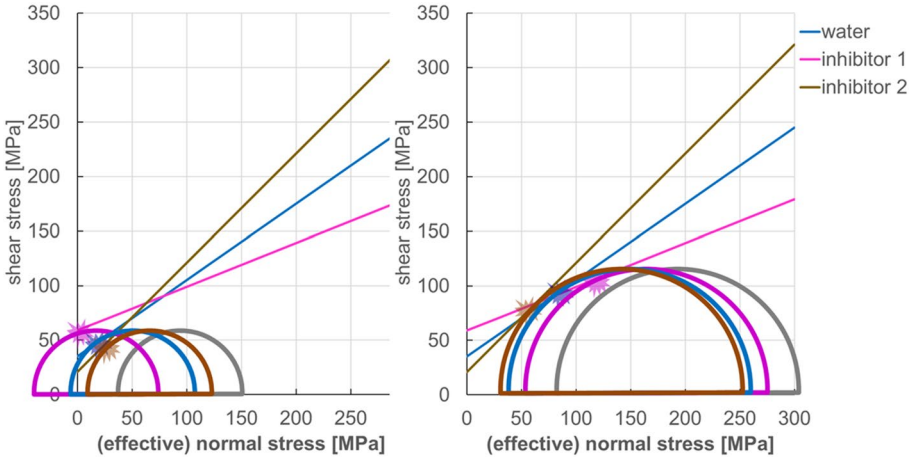

Fig. 8 Imaginary stress initial stress states (grey) shifted towards the origin of a Mohr–Coulomb failure envelope, showing that failure depends on the initial stress state and on which fluid has leaked into the reservoir

When planning a geothermal well, characterisation of reservoir conditions and subsurface geophysical information can help optimize geothermal project planning and reduce the risk of well failure (Daniilidis et al. 2021; Finger and Blankenship 2012). Our findings suggest that rock strength depends not only on confining pressure—and thus depth—but also on fluid type, this could lead to unexpected failure when fluids would leak into the reservoir (this effect is illustrated in Fig. 8). The depth of geothermal reservoirs in the Netherlands ranges from 1.5 to 3 km (Watering and Veld 2019). Horizontal stresses in the Netherlands at 3 km depth are postulated to reach over 40 MPa (Mechelse 2017). This value is slightly above the maximum confining pressure tested here. Different limestone types may exhibit a different brittle-ductile transition, and thereby a different potential for fluid–rock interaction. Our findings indicate that high concentrations of inhibitor would lead to significant changes. A steady leak into the reservoir during 2 or 3 years of production could lead to such concentrations, which is a short period compared to the decades of lifetime projected for most geothermal doublets. Future research should include if there is a critical concentration at which mechanochemical effects of inhibitor on limestone become significant. Moreover, a full hazard and operability analysis in limestone reservoirs should include the potential for leakage and a determination of the likelihood of scenarios under which a concentration build-up could occur.

Conclusion

We set out to experimentally investigate whether mechanical rock properties are affected by exposure to corrosion inhibitors that are commonly used in a geothermal production setting. This was done by performing triaxial compressive tests on Bentheim sandstone or Treuchtlinger Marmor limestone samples that were saturated with inhibitor solutions versus samples saturated with demineralized water. We found the following:

Sandstone exposure to the different inhibitors had no effect on the maximum supported peak stress before failure or Young's Modulus, and correspondingly no effect on the Mohr–Coulomb failure criterion parameters cohesion and friction coefficient. The

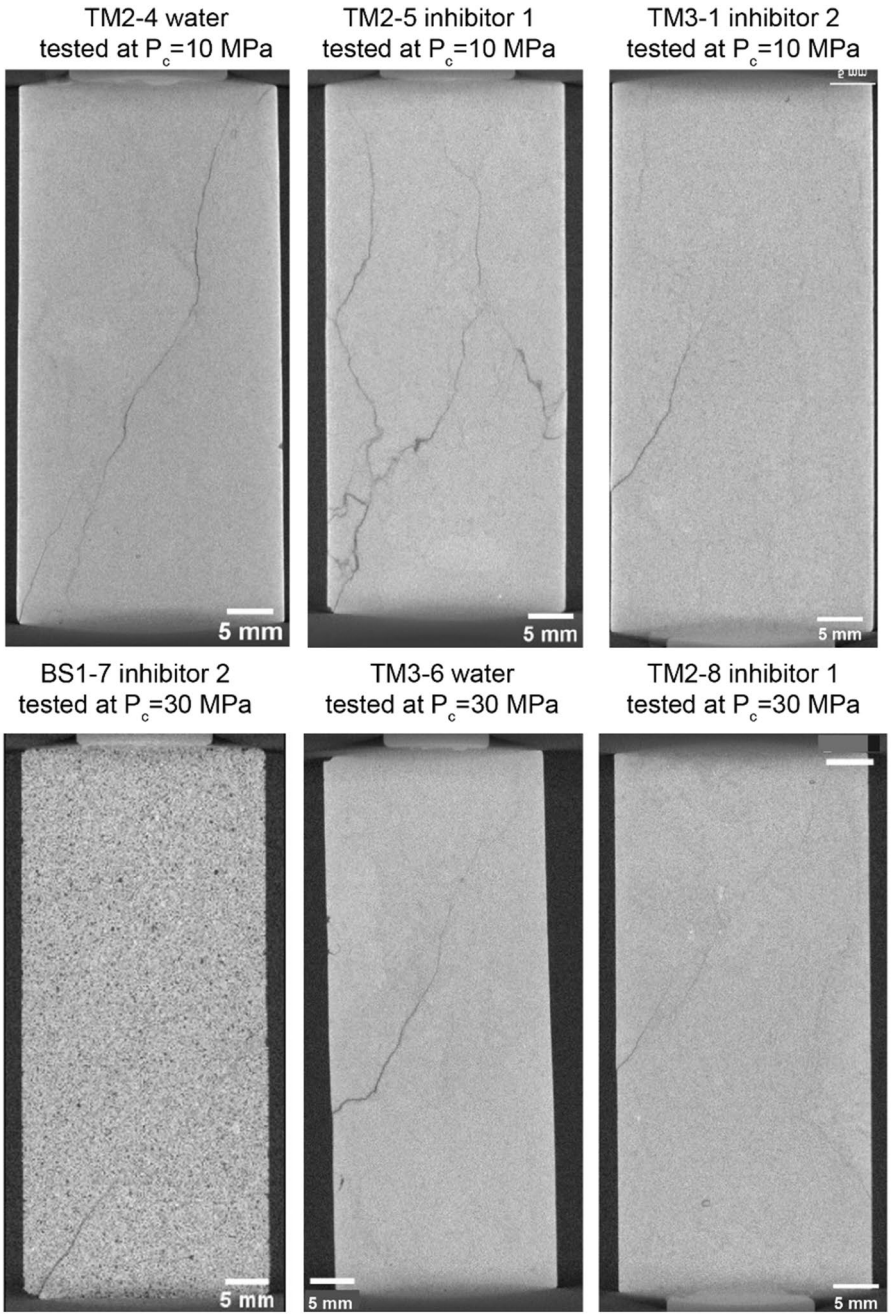

Fig. 9 Overview of 2D slices of the samples scanned with microtomography. At this scale, there is no discernible systematic difference in fracture patterns between samples exposed to different fluid types

cohesion exhibited by Bentheim sandstone samples exposed to demineralized water or inhibitor solution was 19 MPa, the Mohr–Coulomb friction coefficient was 0.80, and the Young's modulus for individual experiments varied between 21.6 and 25.1 GPa. The lack of change with exposure to inhibitor is attributed to the chemically inert nature of the quartz grains.

Limestone exposure to corrosion inhibitors led to significant changes in maximum supported peak stress, though without any systematic effect on Young's modulus

(39.1–52.7 GPa). The two tested inhibitors led to opposite effects on cohesion and friction coefficient. Limestone samples saturated with demineralized water exhibited a cohesion of 33 MPa and a friction coefficient of 0.67. Inhibitor 1 increased cohesion to 59 MPa but decreased the friction coefficient to 0.43, and inhibitor 2 decreased cohesion to 23 MPa, but increased the friction coefficient to 1.01. Microstructural investigation of samples tested at a confining pressure of 20 MPa shows a decreased grain size reduction and increased localization going from demineralized water to inhibitor 1 to inhibitor 2. These changes in limestone strength are attributed to the reactivity of carbonate, the main component of limestone. However, the exact cause for this interaction between the limestone and inhibitor fluids is not yet fully understood. Potential explanations include local dissolution of flaws, leading to more blunt flaw-edges and thereby less easy crack propagation, and/or a change in properties of the fluid film in the grain boundaries, e.g., a local change in viscosity which may affect the intergranular friction coefficient, or a change in zeta potential, changing the attractive and repulsive forces between grain surfaces. This conclusion is important to the geothermal community, since it implies an a priori estimate of reactivity can be made if an effect on rock mechanics should be expected given the reservoir geology and pore fluids expected downhole.

Appendix

3-D X-ray Appendix

Several samples tested at 10 and 30 MPa were scanned (see Table 2; Fig. 9). The only sandstone sample scanned in 3-D was BS07, tested at 30 MPa, since the rest fell apart upon removal from the vessel. This sample exhibited one clean shear fracture, with a location-dependent aperture (higher near the sample boundaries; see Fig. 9d). The limestone samples at low confining pressure exhibit a fracture network of variable fracture density (Fig. 9a–c), and the samples tested at 30 MPa exhibited one clean shear fracture (Fig. 9e–f). With the scale of observation possible using the CT scanner, there is no obvious systematic difference between the fluid types, nor any obvious correlation between microstructure and strength.

Abbreviations

ADBAC	Alkyl dimethylbenzyl ammonium chloride
ϵ_1	Axial strain
BSL	Bentheimer sandstone
ISCO	Brand name for Teledyne ISCO manufactures
$CaCO_3$	Calcium carbonate
dL	Change in sample length
S_0	Cohesion
CT	Computerized tomographic scans
c_i	Concentration of injected corrosion inhibitor
Pc	Confining pressure
DI water	Deionized water
c_d	Downhole concentration of corrosion inhibitor
μ	Friction coefficient
GPa	Giga Pascal
LVDT	Linear variable differential transformer
MPa	Mega Pascal
L_0	Original length
ppm	Parts per million
φ	Porosity

pH	Potential of hydrogen
σ_i	Principal normal stress
r	Radius of deposition
h	Reservoir height
τ	Shear stress
TS	Thin section
TM	Treuchtlinger Marmor
wt%	Weight percentage
E	Youngs Modulus

Acknowledgements
The authors would like to thank Detlev Tondeera of the TU Bergakademie Freuberg and Guido Blöcher of the GeoForschungsZentrum Potsdam for the Treuchtlinger Marmor sample. We would also like to thank the technical support team of Delft University of Technology for help with sample preparation and CT scanning.

Author contributions
AP conceived the presented idea. JDK performed the laboratory experiments and the subsequent data processing under supervision of AP. AP performed the analysis with optical microscopy. JDK wrote the manuscript with support from AB and AP. All authors read and approved the final manuscript.

Funding
This research was partially funded by the Dutch Foundation for Scientific Research (NWO) (Grant Number 016.Veni.181.036) and by NWO Science domain (NWO-ENW), project DEEP.NL.2018.048.

Availability of data and materials
Additional data are available in the additional information files. The datasets used, analysed or generated during the current study are available from the corresponding author on a reasonable request.

Declarations

Competing interests
The authors declare no competing interests.

Received: 10 March 2022 Accepted: 4 May 2023
Published online: 08 June 2023

References

Arson C, Vanorio T. Chemo-mechanical evolution of pore space in carbonate microstructures upon dissolution: linking pore geometry to bulk elasticity. J Geophys Res Solid Earth. 2015;80:WA49–59. https://doi.org/10.1002/2015JB012087.

Atkinson BK, Meredith PG. Stress corrosion cracking of quartz: a note on the influence of chemical environment. Tectonophysics. 1981;77:T1–11. https://doi.org/10.1016/0040-1951(81)90157-8.

Bakker RR, Barnhoorn A. Multiscale evaluation of potential damage in jetted lateral boreholes. Int J Rock Mech Min Sci. 2019;121:104007. https://doi.org/10.1016/j.ijrmms.2019.03.027.

Barnhoorn A, Cox SF, Robinson DJ, Senden T. Stress- and fluid-driven failure during fracture array growth: Implications for coupled deformation and fluid flow in the crust. Geology. 2010;38:779–82. https://doi.org/10.1130/G31010.1.

Bassioni G, Taha Taqvi S. Wettability studies using zeta potential measurements. J Chem. 2015. https://doi.org/10.1155/2015/743179.

Baud P, Zhu W, Wong T. Failure mode and weakening effect of water on sandstone. J Geophys Res Solid Earth. 2000;105:16371–89. https://doi.org/10.1029/2000JB900087.

Baud P, Wong T, Zhu W. Effects of porosity and crack density on the compressive strength of rocks. Int J Rock Mech Min Sci. 2014;67:202–11. https://doi.org/10.1016/J.IJRMMS.2013.08.031.

Blöcher G, Reinsch T, Hassanzadegan A, Milsch H, Zimmermann G. Direct and indirect laboratory measurements of poroelastic properties of two consolidated sandstones. Int J Rock Mech Min Sci. 2014;67:191–201. https://doi.org/10.1016/j.ijrmms.2013.08.033.

Bowen WR, Yousef HNS. Effect of salts on water viscosity in narrow membrane pores. J Colloid Interface Sci. 2003;264:452–7. https://doi.org/10.1016/S0021-9797(03)00406-5.

Boxem T, Veldkamp H, Carpentier S, Goldberg T, Lipsey L. Eindrapport Ultra-diepe geothermie in Nederland. Utrecht: TNO; 2015.

Bruno MS, Nelson RB. Microstructural analysis of the inelastic behavior of sedimentary rock. Mech Mater. 1991;12:95–118. https://doi.org/10.1016/0167-6636(91)90057-7.

Buijze L, van Bijsterveldt L, Cremer H, Paap B, Veldkamp H, Wassing B, van Wees J-D, ter Heege J. Review of worldwide geothermal projects: mechanisms and occurrence of induced seismicity. Utrecht: TNO; 2019.

Carbillet L, Heap MJ, Baud P, Wadsworth FB, Reuschlé T. Mechanical compaction of crustal analogs made of sintered glass beads: the influence of porosity and grain size. J Geophys Res Solid Earth. 2021. https://doi.org/10.1029/2020JB021321.

Castagna A, Ougier-Simonin A, Benson PM, Browning J, Walker RJ, Fazio M, Vinciguerra S. Thermal damage and pore pressure effects on brittle-ductile transition of comiso limestone. J Geophys Res Solid Earth. 2018;123:7644–60. https://doi.org/10.1029/2017JB015105.

Clark AC, Vanorio T. The rock physics and geochemistry of carbonates exposed to reactive brines. J Geophys Res Solid Earth. 2016;121:1497–513. https://doi.org/10.1002/2015JB012445.
Connors KA. Chemical kinetics: the study of reaction rates in solution. Weinheim: VCH; 1990.
Daniilidis A, Khait M, Saeid S, Bruhn DF, Voskov D. A high performance framework for the optimization of geothermal systems, comparing energy production and economic output, in: world geothermal congress. 2021; p. 10.
Descamps F, Ramos M, Schroeder C, Verbrugge J, Tshibangu J. International journal of rock mechanics & mining sciences limiting envelopes of a dry porous limestone under true triaxial stress states. Int J Rock Mech Min Sci. 2012;56:88–99. https://doi.org/10.1016/j.ijrmms.2012.07.013.
Dobereiner L, Freitas MD. Geotechnical properties of weak sandstones. Geotechnique. 1986;36(1):79–94.
Dubelaar C, Nijland TG. The Bentheim sandstone: geology, petrophysics, varieties and its use as dimension stone. In: Lollino G, Giordan D, Marunteanu C, Christaras B, Yoshinori I, Margottini C, editors. Engineering geology for society and territory, vol. 8. Cham: Springer International Publishing; 2015. p. 557–63.
Dutch Association of Geothermal Operators (DAGO), Stichting Platform Geothermie, Stichting Warmtenetwerk and Energie Beheer Nederland B.V. (EBN), 2018. Masterplan Aardwarmte Nederland. https://kennisbank.ebn.nl/het-masterplan-aardwarmte-nederland/
Egert R, Seithel R, Kohl T, Stober I. Triaxial testing and hydraulic–mechanical modeling of sandstone reservoir rock in the Upper Rhine Graben. Geotherm Energy. 2018. https://doi.org/10.1186/s40517-018-0109-0.
Finger JT, Blankenship DA. Handbook of best practices for geothermal drilling (No. SAND2011–6478). Albuquerque, NM: Sandia National Lab (SNL-NM); 2012.
Fischer-cripps AC. Introduction to contact mechanics. New York: Springer; 2000. https://doi.org/10.1007/b97709.
Fossen H. Structural geology. Cambridge: Cambridge University Press; 2010.
Ghaziof S, Zealand N, Osato K, Kasai K, Sakura K, Lichti K, Zealand N, Sato M, Yanagisawa N, Energy R, Fukui T. Application of corrosion inhibitors for K55 casing corrosion control in acidic geothermal well fluids. 2018; pp. 1–12.
Hadizadeh J, Law RD. Water-weakening of sandstone and quartzite deformed at various stress and strain rates. Int J Rock Mech Min Sci. 1991;28:431–9. https://doi.org/10.1016/0148-9062(91)90081-V.
Hallbauer DK, Wagner H, Cook NGW. Some observations concerning the microscopic and mechanical behaviour of quartzite specimens in stiff, triaxial compression tests. Int J Rock Mech Min Sci. 1973;10:713–26. https://doi.org/10.1016/0148-9062(73)90015-6.
Heap MJ, Baud P, Meredith PG, Bell AF, Main IG. Time-dependent brittle creep in darley dale sandstone. J Geophys Res Solid Earth. 2009. https://doi.org/10.1029/2008JB006212.
Heap MJ, Reuschlé T, Kushnir ARL, Baud P. The influence of hydrothermal brine on the short-term strength and elastic modulus of sandstones from exploration well EPS-1 at Soultz-sous-Forêts (France). Geotherm Energy. 2018;6:29. https://doi.org/10.1186/s40517-018-0116-1.
Heggheim T, Madland MV, Risnes R, Austad T. A chemical induced enhanced weakening of chalk by seawater. J Pet Sci Eng. 2005;46:171–84. https://doi.org/10.1016/j.petrol.2004.12.001.
Hilner E, Andersson MP, Hassenkam T, Matthiesen J, Salino PA, Stipp SLS. The effect of ionic strength on oil adhesion in sandstone–the search for the low salinity mechanism. Sci Rep. 2015;5:1–9.
Hoek E, Franklin JA. Simple triaxial cell for field or laboratory testing of rock. Trans Inst Min Metall. 1968;77:A22-26.
Hoek E, Martin CD. Fracture initiation and propagation in intact rock—a review. J Rock Mech Geotech Eng. 2014;6:287–300. https://doi.org/10.1016/J.JRMGE.2014.06.001.
Hoshino K. Effect of porosity on the strength of the clastic sedimentary rocks, in: proceedings of the 3rd Congress of the International Society for Rock Mechanics, Denver, CO. 1974; pp. 511–516.
Huttenloch P, Zorn R, Steger H, Schilling F, Hater W. Performance of corrosion inhibitors on carbon steel in the geothermal environment of the Upper Rhine Graben (URG) depending on inhibitor concentration, temperature and hydrodynamic conditions—a laboratory study. Geothermics. 2021;92:102047. https://doi.org/10.1016/j.geothermics.2021.102047.
Jada A, Akbour RA, Douch J. Surface charge and adsorption from water onto quartz sand of humic acid. Chemosphere. 2006;64:1287–95.
Jaeger, J.C., Cook, N.G.W., Zimmerman, R.W., 2007. Fundamentals of Rock Mechanics, Fourth. ed, Angewandte Chemie International Edition, 6(11), 951–952. Blackwell Publishing Ltd, Victoria.
Kelland MA. Production chemicals for the oil and gas industry. Boca Raton: CRC Press; 2014.
Kelsall, P.C., Watters, R.J., Franzone, J.G., others, 1986. Engineering characterization of fissured, weathered dolerite and vesicular basalt, in: The 27th US Symposium on Rock Mechanics (USRMS).
Klein E, Baud P, Reuschlé T, Wong TF. Mechanical behaviour and failure mode of Bentheim sandstone under triaxial compression. Phys Chem Earth Part A Solid Earth Geod. 2001;26:21–5. https://doi.org/10.1016/S1464-1895(01)00017-5.
Klein E, Reuschlé T, Reuschle T. A model for the mechanical behaviour of bentheim sandstone in the Brittle Regime. In: Kümpel H-J, editor. Thermo-hydro-mechanical coupling in fractured rock. Basel: Birkhäuser Basel; 2003. p. 833–49. https://doi.org/10.1007/978-3-0348-8083-1_3.
Koch, R., Weiss, C., 2005. Field trip A: basin-platform transitions in Upper Jurassic limestones and dolomites of the northern Franconian Alb (Germany). Zitteliana 43–56.
Lisabeth HP, Zhu W. Effect of temperature and pore fluid on the strength of porous limestone. J Geophys Res Solid Earth. 2015;9:6191–208. https://doi.org/10.1002/2015JB012152.
Mackenzie FT, Gees R. Quartz: synthesis at earth-surface conditions. Science. 1971;173:533–5.
Madland MV, Hiorth A, Omdal E, Megawati M, Hildebrand-Habel T, Korsnes RI, Evje S, Cathles LM. Chemical alterations induced by rock-fluid interactions when injecting brines in high porosity chalks. Transp Porous Media. 2011;87:679–702. https://doi.org/10.1007/s11242-010-9708-3.
McMahon AJ. The mechanism of action of an oleic imidazoline based corrosion inhibitor for oilfield use. Colloids Surf. 1991;59:187–208.
Mechelse E. The in-situ stress field in the Netherlands: regional trends, local deviations and an analysis of the stress regimes in the northeast of the Netherlands. 2017.

Megawati M, Hiorth A, Madland MV. The impact of surface charge on the mechanical behavior of high-porosity chalk. Rock Mech Rock Eng. 2013;46:1073–90.
Mijnlieff H. Introduction to the geothermal play and reservoir geology of the Netherlands. Neth J Geosci. 2020;99:E2. https://doi.org/10.1017/njg.2020.2.
Moeck IS, Dussel M, Weber J, Schintgen T, Wolfgramm M. Geothermal play typing in Germany, case study Molasse Basin: a modern concept to categorise geothermal resources related to crustal permeability. Netherlands J Geosci. 2020. https://doi.org/10.1017/njg.2019.12.
Mönnig E. Der Jura von Norddeutschland in der Stratigraphischen Tabelle von Deutschland 2002. Newsletters Stratigr. 2006;41:253–61. https://doi.org/10.1127/0078-0421/2005/0041-0253.
Morgenstern NR, Eigenbrod KD. Classification of argillaceous soils and rocks. J Geotech Eng Div. 1974;100(10):1137–56.
Mundhenk N, Huttenloch P, Sanjuan B, Kohl T, Steger H, Zorn R. Corrosion and scaling as interrelated phenomena in an operating geothermal power plant. Corros Sci. 2013;70:17–28. https://doi.org/10.1016/j.corsci.2013.01.003.
Niebuhr B, Pürner T. Plattenkalk und Frankendolomit ? Lithostratigraphie der Weißjura-Gruppe der Frankenalb (außeralpiner Oberjura, Bayern). Schriftenr Der Dtsch Gesellschaft Für Geowissenschaften. 2014;83:5–72. https://doi.org/10.1127/sdgg/83/2014/5.
Nogara J, Zarrouk SJ. Corrosion in geothermal environment: part 1: fluids and their impact. Renew Sustain Energy Rev. 2018;82:1333–46. https://doi.org/10.1016/j.rser.2017.06.098.
Peksa AE, Wolf KKHAA, Zitha PLJJ. Bentheimer sandstone revisited for experimental purposes. Mar Pet Geol. 2015;67:701–19. https://doi.org/10.1016/j.marpetgeo.2015.06.001.
Plummer LN, Busenberg E. The solubilities of calcite, aragonite and vaterite in CO2-H2O solutions between 0 and 90°C, and an evaluation of the aqueous model for the system CaCO3-CO2-H2O. Geochim Cosmochim Acta. 1982;46:1011–40. https://doi.org/10.1016/0016-7037(82)90056-4.
Pluymakers A, Ougier-Simonin A, Barnhoorn A. Ion-species in pore fluids with opposite effects on limestone fracturing. Geomech Energy Environ. 2021;26:100233. https://doi.org/10.1016/j.gete.2021.100233.
Pvrikryl R. Some microstructural aspects of strength variation in rocks. Int J Rock Mech Min Sci. 2001;38:671–82.
Regnet JB, David C, Fortin J, Robion P, Makhloufi Y, Collin PY. Influence of microporosity distribution on the mechanical behavior of oolithic carbonate rocks. Geomech Energy Environ. 2015;3:11–23. https://doi.org/10.1016/J.GETE.2015.07.002.
Rimstidt JD, Barnes HL. The kinetics of silica-water reactions. Geochim Cosmochim Acta. 1980;44:1683–99. https://doi.org/10.1016/0016-7037(80)90220-3.
Rostom F, Røyne A, Dysthe DK, Renard F. Effect of fluid salinity on subcritical crack propagation in calcite. Tectonophysics. 2013;583:68–75.
Rudnicki JW. Shear and compaction band formation on an elliptic yield cap. J Geophys Res. 2004;109:1–10. https://doi.org/10.1029/2003jb002633.
Rutter EH. The influence of interstitial water on the rheological behaviour of calcite rocks. Tectonophysics. 1972a;14:13–33. https://doi.org/10.1016/0040-1951(72)90003-0.
Rutter EH. The effects of strain-rate changes on the strength and ductility of Solenhofen limestone at low temperatures and confining pressures. Int J Rock Mech Min Sci Geomech Abstr. 1972;9:183–9.
Rutter EH, Glover CT. The deformation of porous sandstones; are Byerlee friction and the critical state line equivalent? J Struct Geol. 2012;44:129–40. https://doi.org/10.1016/j.jsg.2012.08.014.
Shehata AM, Nasr-El-Din HA, others. Zeta potential measurements: impact of salinity on sandstone minerals, in: SPE international symposium on oilfield chemistry. 2015.
Sjöberg EL, Rickard DT. Temperature dependence of calcite dissolution kinetics between 1 and 62°C at pH 2.7 to 8.4 in aqueous solutions. Geochim Cosmochim Acta. 1984;48:485–93. https://doi.org/10.1016/0016-7037(84)90276-X.
Vialle S, Vanorio T. Laboratory measurements of elastic properties of carbonate rocks during injection of reactive CO_2 -saturated water. Geophys Res Lett. 2011. https://doi.org/10.1029/2010GL045606.
van de Watering, F., van der Veld, R., 2019. (Environmental) impact of inhibitors applied in the geothermal sector In The Netherlands, in: European Geothermal Congress.
Yang S-Q, Jing H-W, Wang S-Y. Experimental investigation on the strength, deformability, failure behavior and acoustic emission locations of red sandstone under triaxial compression. Rock Mech Rock Eng. 2012;45:583–606.
You M. Three independent parameters to describe conventional triaxial compressive strength of intact rocks. J Rock Mech Geotech Eng. 2010;2:350–6.
Zhang J, Wong T-F, Davi DM. Micromechanics of pressure-induced grain crushing in porous rocks. J Geophys Res. 1990;95:341–52. https://doi.org/10.1029/JB095iB01p00341.
Zhu W, Montesi LGJ, Wong TF. Shear-enhanced compaction and permeability reduction: triaxial extension tests on porous sandstone. Mech Mater. 1997;25:199–214. https://doi.org/10.1016/S0167-6636(97)00011-2.
Zotzmann J, Vetter A, Regenspurg S. Evaluating efficiency and stability of calcite scaling inhibitors at high pressure and high temperature in laboratory scale. Geotherm Energy. 2018. https://doi.org/10.1186/s40517-018-0105-4.

Publisher's Note